

A Protection-Interoperable Fault Ride-Through Control for Grid-Forming Inverters

Yifei Li, Student Member, IEEE, Heng Wu, Senior Member, IEEE, Xiongfei Wang, Fellow, IEEE

Abstract—Differing from synchronous generators (SGs), grid-forming inverter-based resources (GFM-IBRs) exhibit rapid variations in their output impedances during transmission line faults due to the overcurrent limitation. As a result, the source dynamics during the fault period deviate significantly from those under pre-fault conditions. This fundamental difference alters the fault responses of incremental quantities, thereby jeopardizing the reliability of the supervising elements in protective relays that are based on these quantities. To address this challenge, a protection-interoperable fault ride-through (FRT) method for GFM-IBRs is proposed. This method dynamically adjusts power control of GFM-IBRs in response to the changes in output impedance, effectively mitigating variations in source dynamics and thereby preserving the reliability of incremental quantity-based supervising elements. This method also ensures effective overcurrent limitation and transient stability of GFM-IBRs. Controller hardware-in-the-loop (CHIL) and experimental tests validate the effectiveness of the proposed method.

Index Terms—Grid forming, inverter-based resources, protection-interoperable control, supervising elements.

I. INTRODUCTION

GRID-forming inverter-based resources (GFM-IBRs) are treated as a promising substitute technology for synchronous generators (SGs) in future power systems with high penetration of renewable energy power generation [1], [2]. However, deploying GFM-IBRs at large scale can significantly alter fault characteristics of power systems, which may further affect the reliability of the protective relays that are designed for legacy SG-based power systems [3], [4].

Supervising elements, including directional and phase selection elements, are standard elements that are integrated into protective relays to ensure tripping occurs only for faulted phases during a forward fault [3], [5], thereby enhancing the resilience and reliability of power systems [6], [7]. To eliminate the impact of load conditions, the phase angle characteristics of incremental quantities, i.e., the incremental voltage and current, are commonly employed in supervising elements for assessing the faulted phases and the direction of the fault [8], [9], [10]. The operation of these incremental quantity-based supervising elements is built on the compensation theory, which assumes that the variations of source dynamics, including the internal voltage source (IVS) and output impedance dynamics, are negligible during the fault period when compared to pre-fault conditions [11], [12]. For GFM-IBRs, the variations in IVS dynamics are negligible under the typical slow-timescale power control [2]. However, due to overcurrent limitations, the GFM-IBRs undergo rapid changes in their output impedances

during the fault period, which is different from SGs [3]. This distinction results in the source dynamics during the fault period differing significantly from those before the fault. Consequently, the phase angle characteristics of incremental quantities are altered, jeopardizing the reliability of the incremental quantity-based supervising elements.

To ensure reliable operations of incremental quantity-based supervising elements, either the protective algorithm or the control scheme of the IBR should be modified [13]. Given the continuous evolution of IBR characteristics driven by updates of grid codes, one promising solution for the modification of protective algorithm is to make it decoupled from the source characteristics [13], [14]. For instance, the SEL-T400L employs traveling waves to determine the direction of the fault and time-domain quantities to identify the faulted phases [15]. While these methods operate mostly independently of the source characteristics, they require a high sampling rate of 1 MHz, posing challenges for hardware implementation [15]. Further, updating all these protective elements increases the economic cost [6], [16]. Therefore, implementing protection-interoperable control to ensure the compatibility of GFM-IBRs with the conventional supervising elements presents a cost-effective and attractive solution [17].

In [7], the current reference generation of IBRs is adjusted according to the tripping criteria of the directional elements to enhance reliability. Similarly, in [6] and [18], the control schemes are adjusted according to the tripping criteria of the phase selection elements. However, modifying control schemes to be adapted to one protective element may adversely impact the reliability of other elements. The unified requirements for both directional and phase selection elements are thus needed to effectively modify the control schemes of IBRs. Moreover, most previous studies focus on modifying the grid-following (GFL) control [4]. Unlike GFL-IBRs, GFM-IBRs operate as IVSs behind output impedances, exhibiting high stability in weak grids [2], [19]. However, the protection-interoperable control methods for GFM-IBRs remain largely underexplored [4].

Beyond meeting the requirements of protective relays, IBRs should also reliably ride through grid faults while accounting for overcurrent limitations and transient stability [20], [21]. In [1], the steady-state fault current is limited by adjusting the power references, and the transient fault current is limited by using the virtual resistor control. The effects of various current limiting controls (CLCs) on transient stability and dynamic behavior of IBRs are summarized in [21]. An adaptive fast/slow control method is introduced in [2], which guarantees the transient stability of GFM-IBRs. While the CLC and the transient stability are thoroughly studied in [1], [2], [20], and

[21], these works do not consider the impact of control strategies on the reliability of supervising elements.

To bridge the above-mentioned gaps, this paper proposes a protection-interoperable FRT method for GFM-IBRs, which assures reliable operations of the incremental quantity-based supervising elements and effectively meets the requirements of overcurrent limitations and transient stability of GFM-IBRs, all are essential control targets. **In contrast, the transient stability is often overlooked in prior studies that primarily focus on the reliable operation of protective relays [6], [7], [18], while the protective relays are seldom mentioned in the studies on transient stability [2].** The key aspects of the protection-interoperable FRT method are as follows:

- 1) The power control of IBRs is modified such that source dynamics, including the dynamics of IVS and output impedance, in the fault sequence network remain equivalent to those in the pre-fault operation, thereby maintaining reliable operations of supervising elements that are based on incremental quantities.
- 2) The modified power control operates in an open-loop manner and is activated exclusively during the operation of the supervising elements, whereas at all other times, the closed-loop power control is employed to maintain synchronization of the IBR with the grid. The transition between these two modes is governed by the switching criteria, which are designed based on the comparison of current magnitude against predefined thresholds and the operating duration of supervising elements.
- 3) The requirements for preventing overcurrent during IBR operation under the modified power control, imposed on the output impedance shaped by the CLC, are established.

The advantages of the proposed method are listed below:

- 1) The method ensures reliable operations of both incremental quantity-based directional and phase selection elements.
- 2) With the open-loop power control adopted initially after the fault inception, and the adaptive fast/slow control [2] used during fault recovery, the proposed method assures the transient stability of GFM-IBRs.

Lastly, the controller hardware-in-the-loop (CHIL) tests and experiments validate the effectiveness of the proposed method.

II. PRECONDITIONS OF SUPERVISING ELEMENTS

This section briefly reviews the operating principles of supervising elements used in power system protection, based on which the preconditions for their reliable operation are summarized.

A. Principle of Supervising Elements

Fig. 1 shows the single-SG infinite bus system. Here, v , i , and v_e , i_g represent the voltages and currents at the bus 1 and the bus 2, respectively. Z_l denotes the transmission line impedance. Fault points in the reverse and forward directions are marked as F_x and F_y , respectively. R_1 and R_2 are the distance relays that incorporate the distance elements and supervising elements, including directional and phase selection elements. The bcg

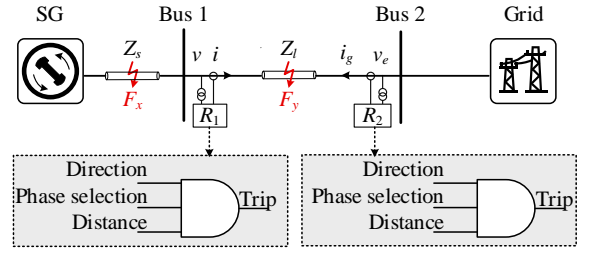


Fig. 1 Single-SG infinite bus system.

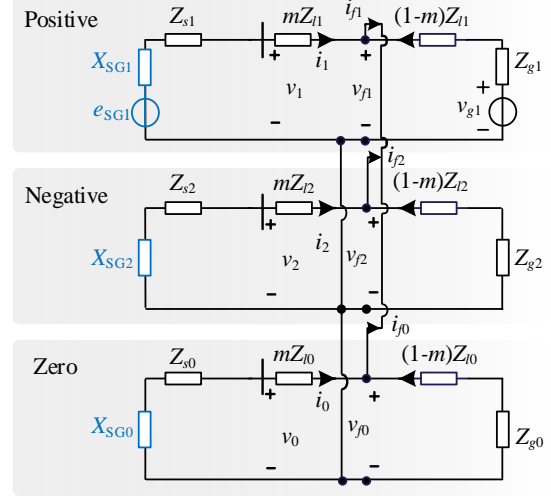


Fig. 2 Sequence network under a bcg fault in the single SG-based power system.

(phase b to phase c to ground) fault at F_y is used as an example to illustrate the principle of supervising elements.

1) Principle of directional element

Fig. 2 depicts the corresponding fault sequence network of Fig. 1, where v_{SG1} denotes the internal voltage of the SG. X_{SG} and Z_g represent the output impedances of the SG and grid, respectively. The symbol m denotes the fault location, and the subscript ' f ' denotes the quantities at the fault location. The subscripts 0, 1, and 2 represent zero-, positive-, and negative-sequence quantities, respectively. Applying Kirchoff's law to the sequence network in Fig. 2, the angle differences between voltages and currents of negative-sequence quantities (φ_2) and zero-sequence quantities (φ_0) are expressed as

$$\begin{cases} \varphi_2 = \angle \frac{v_2}{i_2} = \angle - \frac{(Z_{s2} + jX_{SG2})}{Z_{e2}} \\ \varphi_0 = \angle \frac{v_0}{i_0} = \angle - \frac{(Z_{s0} + jX_{SG0})}{Z_{e0}} \end{cases} \quad (1)$$

where Z_{e2} and Z_{e0} represent the effective impedances. Due to the fact that the output impedances of the SG and transmission line are highly inductive [22], it is known from (1) that a forward fault, e.g., the fault occurs at F_y , results in $\varphi_2 \approx \varphi_0 \approx 90^\circ$. In contrast, in the case of a reverse fault, e.g., the fault occurs at F_x , the fault current holds an opposite phase angle compared to that during the forward fault, and the effective impedances are formed by the grid-side impedances [23], yielding $\varphi_2 \approx \varphi_0 \approx 90^\circ$. Therefore, the values of φ_2 and φ_0 can be used to identify the direction of the fault.

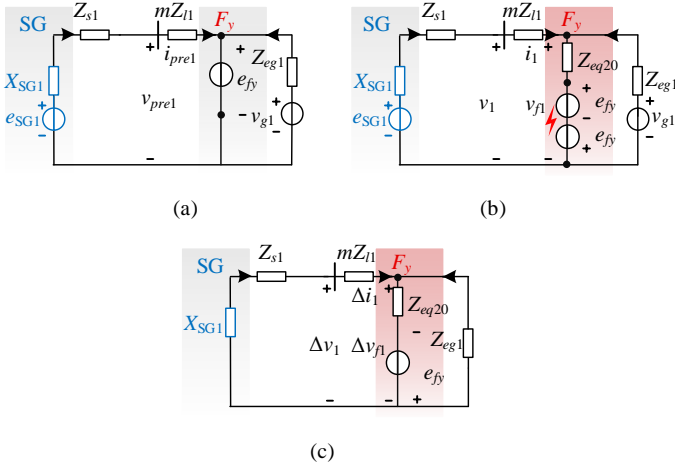


Fig. 3 Illustration of the compensation theory in the SG-based system. (a) Pre-fault circuit. (b) Fault sequence network. (c) Pure-fault sequence network.

However, in the event of a symmetrical fault, the negative- and zero-sequence quantities are absent, leaving only the positive-sequence quantities available for the supervising elements. Nevertheless, the positive-sequence quantities are affected by load conditions [10]. Consequently, the incremental quantities derived based on compensation theory are used instead.

Fig. 3 illustrates the compensation theory in the SG-based system, where $Z_{eg1}=(1-m)Z_{l1}+Z_{g1}$. Z_{eq20} is the equivalent parallel impedance for negative- and zero-sequence circuits. e_{fy} and v_{f1} are the pre-fault and fault voltages at the point F_y , respectively. The subscript 'pre' in Fig. 3 (a) stands for the pre-fault quantities. For analysis of protective relays, the IVS (e_{SG1}) and output impedance (Z_{SG1}) of SGs in the fault sequence network are generally assumed to be similar to those in the pre-fault circuit [3], [11], [22], as shown in Fig. 3 (a) and (b).

Applying nodal analysis to the pre-fault circuit [Fig. 3 (a)] and fault sequence network [Fig. 3 (b)], the voltages at the fault location are separately derived by

$$e_{fy} = \frac{e_{SG1}(Y_{SG1} + Y_{s1} + mY_{l1}) + v_{g1}Y_{eg1}}{Y_{SG1} + Y_{s1} + mY_{l1} + Y_{eg1}} \quad (2)$$

$$v_{f1} = \frac{e_{SG1}(Y_{SG1} + Y_{s1} + mY_{l1}) + v_{g1}Y_{eg1}}{Y_{SG1} + Y_{s1} + mY_{l1} + Y_{eg1} + Y_{eq20}} \quad (3)$$

where the symbol Y stands for admittance. Subtracting (2) from (3), yields

$$\begin{aligned} \Delta v_{f1} &= v_{f1} - e_{fy} \\ &= \frac{-e_{fy}Y_{eq20}}{Y_{SG1} + Y_{s1} + mY_{l1} + Y_{eg1} + Y_{eq20}} \end{aligned} \quad (4)$$

Fig. 3 (c) presents the pure-fault sequence network derived based on (4). Applying Kirchoff's law to the circuit in Fig. 3 (c), the Δi_1 and Δv_1 are expressed as

$$\begin{cases} \Delta i_1 = -\frac{\Delta v_{f1}}{jX_{SG1} + Z_{s1} + mZ_{l1}} \\ = -\frac{v_{f1} - e_{SG1}}{jX_{SG1} + Z_{s1} + mZ_{l1}} - \left(-\frac{e_{fy} - e_{SG1}}{jX_{SG1} + Z_{s1} + mY_{l1}} \right) \\ \Delta v_1 = -\Delta i_1(jX_{SG1} + Z_{s1}) \\ = \underbrace{e_{SG1} - i_1(jX_{SG1} + Z_{s1})}_{v_1} - \underbrace{(e_{SG1} - i_{pre1}(jX_{SG1} + Z_{s1}))}_{v_{pre1}} \end{cases} \quad (5)$$

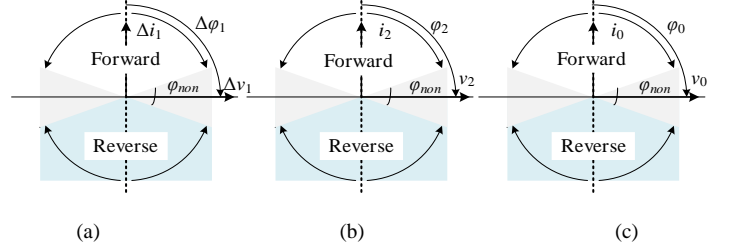


Fig. 4 Phase angle characteristics of directional elements. (a) $\Delta\phi_1$. (b) ϕ_2 . (c) ϕ_0 .

Following (5), Δv_1 and Δi_1 are obtained through the subtraction between the fault quantities (v_1 , i_1) and pre-fault quantities (v_{pre1} , i_{pre1}), and the angle difference between Δv_1 and Δi_1 is given by

$$\Delta\phi_1 = \angle -\frac{\Delta v_1}{\Delta i_1} \approx \angle -\frac{(jX_{SG1} + Z_{s1})}{\Delta Z_{e1}} \quad (6)$$

where ΔZ_{e1} is the effective impedance for the incremental quantities. During a forward fault, based on (6), $\Delta\phi_1 \approx 90^\circ$. During a reverse fault, Δi_1 holds an opposite phase angle to the forward fault, resulting in $\Delta\phi_1 \approx 90^\circ$. Therefore, the value of $\Delta\phi_1$ can also be used to identify the direction of the fault.

Furthermore, in Fig. 3 (c), the e_{SG1} and v_{g1} are removed. Therefore, by using Δv_1 and Δi_1 in Fig. 3 (c), the adverse impact of load conditions on the performance of the supervising elements is eliminated.

Fig. 4 illustrates the principles of the directional elements. The angle differences between voltage and current for the incremental quantities ($\Delta\phi_1$) in Fig. 4 (a), the negative-sequence quantities (ϕ_2) in Fig. 4 (b), and the zero-sequence quantities (ϕ_0) in Fig. 4 (c) are used to identify the direction of the fault. $\Delta\phi_1$, ϕ_2 , and ϕ_0 fall within the reverse or forward zones based on the corresponding direction of the fault. Additionally, the non-tripping zones (ϕ_{non}) are defined within a range of 30° to 60° to improve the reliability of the directional elements [24].

2) Principle of phase selection elements

A one-to-one mapping exists between the angle differences at the fault location [$\delta_{f21}=\angle i_{f2}-\angle i_{f1}$, $\delta_{f20}=\angle i_{f2}-\angle i_{f0}$] and the fault types, forming the foundation for faulted phases identification [10]. However, the relay cannot directly measure the quantities at the fault location. When the output impedances of the sources are highly inductive, the phase angles of the sequence quantities at the relay-assembled point correspond to those at the fault location for negative- and zero-sequence quantities, i.e., $\angle i_2=\angle i_{f2}$, and $\angle i_0=\angle i_{f0}$, enabling identification of faulted phases. For further details, refer to [10] and [11].

However, due to the impact of load conditions, $\angle i_1$ does not necessarily match $\angle i_{f1}$. Since the incremental quantity remains unaffected by load conditions, i.e., $\angle \Delta i_1=\angle i_{f1}$, it can be used to identify the faulted phases [10].

Fig. 5 shows the principles of the phase selection elements. The angle difference between i_2 and Δi_1 ($\Delta\delta_{21}$) shown in Fig. 5 (a), and the angle difference between i_2 and i_0 (δ_{20}) shown in Fig. 5 (b) are used simultaneously to identify faulted phases. To enhance reliability, the fault type zones for $\Delta\delta_{21}$ and δ_{20} are

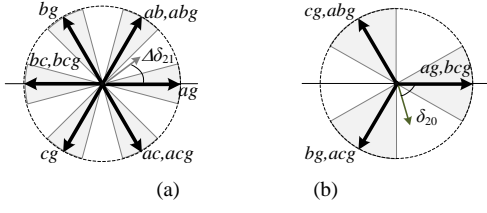
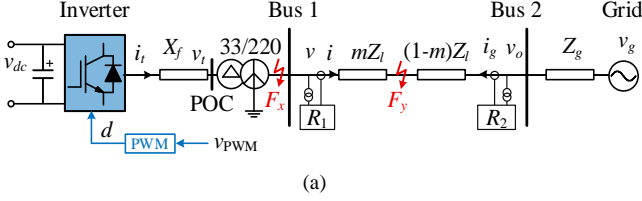
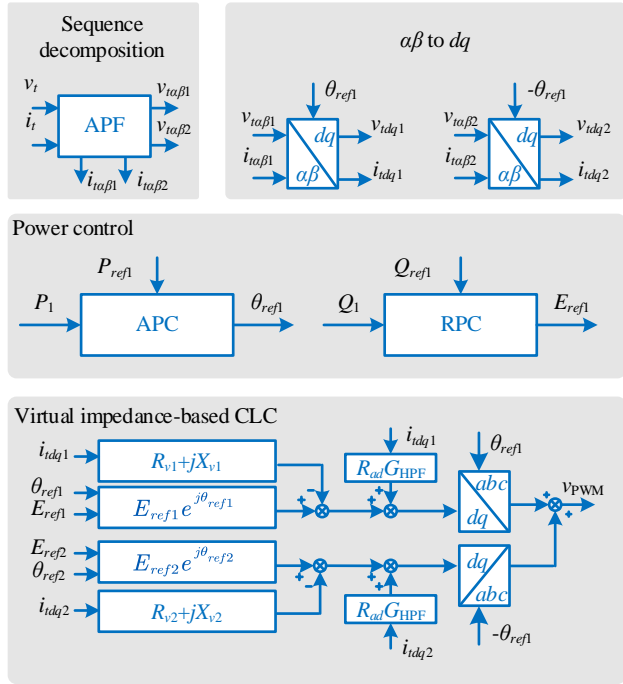


Fig. 5 The principle for PSEs. (a) $\Delta\delta_{21}$. (b) δ_{20} .



(a)



(b)

Fig. 6 Main circuit and control schemes of the single-IBR infinite bus system. (a) Main circuit. (b) Control loops.

extended by $\pm 15^\circ$ and $\pm 30^\circ$, respectively [25].

B. Preconditions

Based on the above analysis, the preconditions for the supervising elements are listed below:

- The effective impedance is highly inductive.
- The difference in source dynamics, including IVS and output impedance dynamics, between the fault sequence network and the pre-fault circuit is negligible.

III. IMPACT OF GFM-IBRS ON SUPERVISING ELEMENTS

A. System Description

Fig. 6 (a) shows the main circuit of the single-IBR infinite bus system. v_i and i_i are the voltage and current at the point of coupling (POC), respectively. X_f represents the filter. A constant DC-link voltage (v_{dc}) is assumed, as it is typically maintained by the front-end converter or an energy storage unit [1].

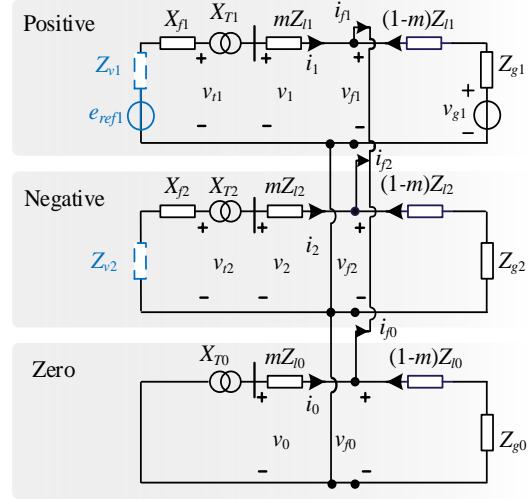


Fig. 7 Sequence network under a bcg fault in GFM-IBR-based systems.

Fig. 6 (b) illustrates the control scheme for the GFM-IBR, where the all-pass filter (APF) is utilized to decompose the positive- and negative-sequence quantities, considering the asymmetrical faults at the transmission line [26]. The power control consists of active power control (APC) and reactive power control (RPC). The APC is used to generate the phase angle reference θ_{ref1} for dq transformation, while the RPC is utilized to generate the positive-sequence voltage magnitude reference (E_{ref1}). To ensure a balanced voltage, the negative-sequence voltage magnitude reference is set as zero, i.e., $E_{ref2}=0$ [27].

To prevent the failure of power semiconductor devices from overcurrent, the virtual impedance-based CLC method is implemented. In this method, the active damping resistor R_{ad} is used to dampen the synchronous resonance introduced by the power control. Moreover, a high-pass filter (G_{HPF}) is cascaded with R_{ad} to eliminate its impact on the steady-state power control performance [2].

B. Impact Analysis

1) X/R ratio of the virtual impedance

Fig. 7 presents the sequence network of Fig. 6 (a) during a bcg forward fault, where $e_{ref1}=E_{ref1} \angle \theta_{ref1}$, and X_T is the leakage reactance of the transformer. Applying Kirchhoff's law to the circuits in Fig. 7, the angle differences between voltages and currents of negative-sequence quantities (φ_2) and zero-sequence quantities (φ_0) are expressed as

$$\begin{cases} \varphi_2 = \angle \frac{v_2}{i_2} = \angle - \underbrace{(n^2 Z_{v2} + jn^2 X_{f2} + jX_{T2})}_{Z_{e2}} \\ \varphi_0 = \angle \frac{v_0}{i_0} = \angle - \underbrace{(jn^2 X_{f0} + jX_{T0})}_{Z_{e0}} \end{cases} \quad (7)$$

where n is the turns ratio of the transformer. Based on (7), Z_{e2} is affected by the virtual impedances. Therefore, it may not be highly inductive, which may cause malfunctions of supervising elements depicted in Fig. 4 and Fig. 5.

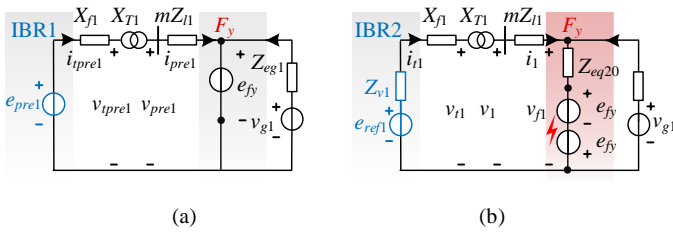


Fig. 8 Illustration of the source dynamic in IBR-based systems. (a) Pre-fault circuit. (b) Fault sequence network.

To address this issue, a highly inductive virtual impedance-based CLC method is implemented to ensure Z_{v2} remains highly inductive. Consequently, Z_{e2} is maintained as highly inductive. However, the performance of incremental quantity-based supervising elements is affected by the source dynamics and should be further investigated.

2) Source dynamics

Fig. 8 illustrates the source dynamics, including IVS and output impedance dynamics, where IBR1 and IBR2 denote the IBR models before and during the fault, respectively. Here, e_{pre1} represents the IVS of the IBR before the fault. Fig. 8 (a) shows that the overcurrent limitation is not triggered before the fault, and the output impedance of the IBR1 is 0. During the fault, with the typically slow-timescale power control, the IVS remains approximately equal to its pre-fault value, i.e., $e_{ref1} \approx e_{pre1}$ [2]. However, when the virtual impedance-based CLC is triggered, an additional impedance Z_{v1} is introduced as the output impedance of the IBR2, as depicted in Fig. 8 (b). Therefore, unlike the SG, the output impedance of the IBR undergoes rapid changes, resulting in mismatched source dynamics between IBR2 in Fig. 8 (b) and IBR1 in Fig. 8 (a). Consequently, the assumption underlying the compensation theory—that the source dynamics remain nearly unchanged—no longer holds.

Directly subtracting the pre-fault quantities in the circuit of Fig. 8 (a) from the fault quantities in the sequence network of Fig. 8 (b), the effective impedance for the incremental quantities is expressed as

$$\begin{aligned} \Delta Z_{e1} &= -\frac{\Delta v_1}{\Delta i_1} = -\frac{v_1 - v_{pre1}}{i_1 - i_{pre1}} \\ &= (jn^2 X_{f1} + jX_{T1}) + \underbrace{\frac{ne_{pre1} - ne_{ref1} + n^2 i_1 Z_{v1}}{i_1 - i_{pre1}}}_{Z_{ad}} \quad (8) \end{aligned}$$

Thanks to the slow-timescale power control, $e_{ref1} \approx e_{pre1}$. However, the phase angle of i_1 does not necessarily match that of $i_1 - i_{pre1}$. Hence, Z_{ad} cannot be ensured highly inductive. Consequently, based on (8), the expected highly inductive ΔZ_{e1} cannot be directly determined by subtracting pre-fault quantities from the fault quantities, which can adversely impact the performance of the incremental quantity-based supervising elements.

C. Challenge

The challenge posed by GFM-IBRs to the performance of supervising elements is, therefore, summarized below:

- Unlike SGs, GFM-IBRs exhibit significantly different source dynamics during fault conditions compared to

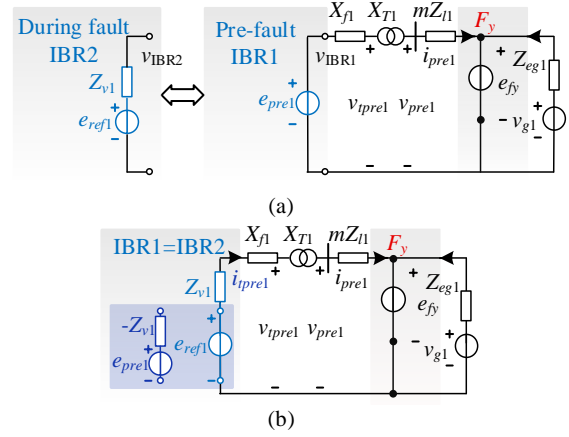


Fig. 9 Illustration of the equivalent dynamics in the pre-fault circuit. (a) Replacement of the IBRs. (b) Equivalent pre-fault circuit.

pre-fault conditions. Consequently, the incremental quantity-based supervising elements cannot be directly applied.

IV. PROTECTION-INTEROPERABLE FRT CONTROL

This section presents first the general idea of protection-interoperable FRT control for GFM inverters, developed to address the identified challenge. Then, the pure-fault circuit for the incremental quantities under this control is derived to demonstrate its effectiveness.

A. General Idea

In SG-based systems, the IVS and output impedance dynamics in the fault sequence network remain nearly unchanged from those in the pre-fault circuit, allowing the expected incremental quantities to be derived by subtracting the pre-fault quantities from the fault quantities. As a result, the incremental quantity-based supervising elements are applicable.

Inspired by the equivalence between SG dynamics in fault sequence networks and pre-fault circuits, a similar principle can be applied to IBR-based systems. Specifically, if IBR2 exhibits equivalent IVS and output impedance dynamics as IBR1, the expected incremental quantities can be obtained based on the compensation theory, enabling the application of incremental quantity-based supervising elements in IBR-based systems.

To achieve this, two approaches are considered:

- Modifying the control scheme during the fault to ensure IBR2 is equivalent to IBR1 in the **fault sequence network**, i.e., setting $ne_{ref1} - n^2 i_1 Z_{v1} = ne_{pre1}$. Under this circumstance, based on (8), the magnitude of Z_{ad} becomes 0, and ΔZ_{e1} is highly inductive. However, the terminal voltage of the IBR during the fault period remains the same as in the pre-fault condition, thereby inherently disabling overcurrent limitation and making this method impractical.
- Modifying the control scheme during the fault to ensure IBR1 is equivalent to IBR2 in the **pre-fault circuit**, i.e., ensuring e_{pre1} remains equivalent to the IVS (e_{ref1}) in series with the virtual impedance (Z_{v1}) in the pre-fault circuit.

Fig. 9 (a) illustrates the equivalent source dynamics in the pre-fault circuit. To ensure that IBR1 is equivalent to IBR2 in

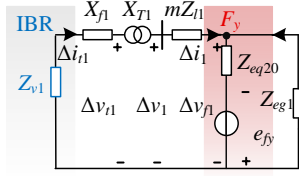


Fig. 10 Pure-fault circuit.

the pre-fault circuit, e_{ref1} is adjusted such that the terminal voltage of IBR2 (v_{IBR2}) matches that of IBR1 (v_{IBR1}), i.e. $e_{ref1} - i_{pre1}Z_{v1} = e_{pre1}$. The IVS during the fault period is adjusted as

$$e_{ref1} = e_{pre1} + i_{pre1}Z_{v1} \quad (9)$$

Fig. 9 (b) depicts the equivalent pre-fault circuit after implementing (9) and replacing IBR1 with IBR2. In Fig. 9 (b), the voltage and the current at the relay-assembled point (the bus 1) are the same as those in the pre-fault circuit shown in Fig. 8 (a).

Substituting (9) into (8), the effective impedance for the incremental quantities is derived by

$$\begin{aligned} \Delta Z_{e1} &= jn^2 X_{f1} + jX_{T1} + \frac{ne_{pre1} - (ne_{pre1} + n^2 i_{pre1} Z_{v1}) + n^2 i_1 Z_{v1}}{i_1 - i_{pre1}} \\ &= jn^2 X_{f1} + jX_{T1} + \frac{ne_{pre1} - ne_{pre1} + n^2 Z_{v1} (i_1 - i_{pre1})}{i_1 - i_{pre1}} \quad (10) \\ &= jn^2 X_{f1} + jX_{T1} + n^2 Z_{v1} \end{aligned}$$

Based on (10), ΔZ_{e1} is highly inductive, indicating that the incremental quantity-based supervising elements can operate reliably after adjusting the IVS based on (9).

B. Pure-Fault Circuit Model

The voltages at the fault location of the fault sequence network, see Fig. 8 (b), and the equivalent pre-fault sequence circuit, see Fig. 9 (b), are separately derived as

$$v_{f1} = \frac{e_{ref1}(Y_{v1}/n^2 + Y_{f1}/n^2 + X_{T1} + mY_{l1}) + v_{g1}Y_{eg1}}{Y_{v1}/n^2 + Y_{f1}/n^2 + X_{T1} + mY_{l1} + Y_{eg1} + Y_{eq20}} \quad (11)$$

$$e_{fy} = \frac{e_{ref1}(Y_{v1}/n^2 + Y_{f1}/n^2 + Y_{f1} + X_{T1} + mY_{l1}) + v_{g1}Y_{eg1}}{Y_{v1}/n^2 + Y_{f1}/n^2 + X_{T1} + mY_{l1} + Y_{eg1}} \quad (12)$$

Subtracting (12) from (11), yields

$$\begin{aligned} \Delta v_{f1} &= v_{f1} - e_{fy} \\ &= \frac{-e_{y1}Y_{eq20}}{Y_{v1} + Y_{f1} + X_{T1} + mY_{l1} + Y_{eg1} + Y_{eq20}} \quad (13) \end{aligned}$$

Fig. 10 presents the pure-fault sequence network based on (13). By adjusting the IVS following (9), the pure-fault circuit of the IBR-based system closely resembles that of SG-based systems shown in Fig. 3 (c), where the load is eliminated.

V. REALIZATION OF PROTECTION-INTEROPERABLE FRT CONTROL

This section elaborates first on the proposed power control for realizing the idea of the protection-interoperable FRT control. The power control operates in two modes: 1) the protection-interoperable mode, where IVS is adjusted according to (9); and 2) the normal mode, where the IVS is regulated via the normal closed-loop power control. Criteria for switching between the two power control modes are then defined. Finally, a CLC method is introduced to ensure the effective overcurrent limitation in the protection-interoperable mode.

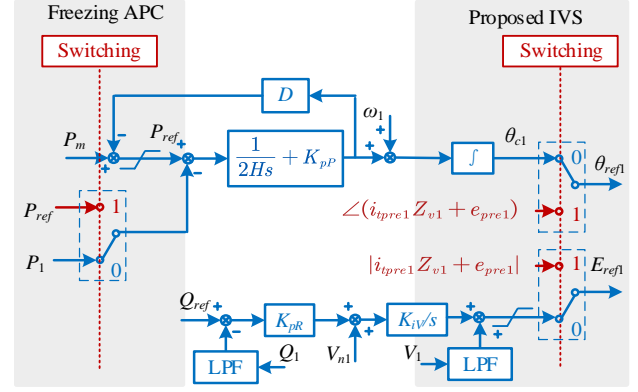


Fig. 11 Proposed power control loop.

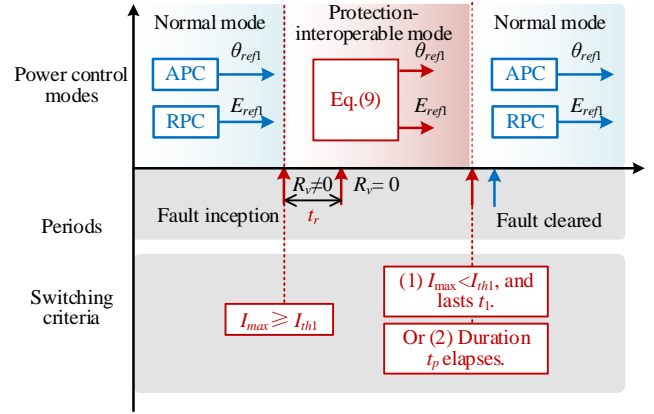


Fig. 12 Control modes for a fault event.

A. Proposed Power Control

Fig. 11 shows the proposed power control to provide the internal voltage based on (9), where ω_1 , V_{n1} are the nominal angular frequency and voltage magnitude, respectively. D , H , and K_{pP} represent the P - ω droop coefficient, the virtual inertia constant, and the virtual damping constant, respectively. The first-order low-pass filter (LPF) is used in RPC to prevent the impact of measurement noise. Before the fault, the output of the APC (θ_{c1}) is determined by the normal power control, which is expressed as

$$\theta_{c1} = ((P_{ref} - P_1)K_{pP} + \omega_1) \frac{1}{s} \quad (14)$$

After the fault inception, the switches generating θ_{ref1} and E_{ref1} in Fig. 11 should shift from port 0 to port 1, activating the protection-interoperable mode. In this case, since $P_{ref} \neq P_1$, the resulting error accumulates in θ_{c1} , as described in (14). When the fault is cleared and the switches return to port 0, this accumulated error can cause an undesirable active power transient. To address this issue, the APC is frozen under the protection-interoperable mode by substituting P_1 with P_{ref} , thereby eliminating the accumulated error in θ_{c1} .

B. Criteria For Switching Between Power Control Modes

Fig. 12 illustrates the transitions between protection-interoperable and normal power control modes, incorporating the associated switching criteria, where I_{max} is expressed as

$$I_{max} = \max(I_{ta}, I_{tb}, I_{tc}) \quad (15)$$

I_{ta} , I_{tb} , and I_{tc} represent the peak values of the phase currents for phases a , b , and c , respectively. For a detailed calculation of

the peak values, refer to [28]. By comparing I_{\max} to a predefined threshold (I_{th1}), the system can determine whether to transition into protection-interoperable mode. To enhance sensitivity and ensure reliability of the relay, I_{th1} is set slightly higher than the nominal current I_{N1} , e.g., $I_{th1}=1.05I_{N1}$. When $I_{\max}\geq I_{th1}$, the protection-interoperable power control is activated.

Once the fault is cleared, the control should transition from protection-interoperable mode back to normal mode. Since the virtual impedance-based CLC method is free of the latch-up phenomenon, the current magnitude can return to the normal level [29]. Consequently, the switching criteria remain based on the POC current magnitude. To prevent frequent switching caused by measurement noises, a time delay of t_1 is introduced. If $I_{\max}<I_{th1}$ for t_1 , the system reverts to port 0 in Fig. 11. However, this delay reduces switching sensitivity. To balance reliability and sensitivity, t_1 should be set properly. In this paper, t_1 is set to 50 ms.

Further, the incremental quantity-based supervising elements store data for a limited time duration, t_p [5]. Once t_p elapses after fault inception, the stored data no longer represent the pre-fault values (i_{pre1} and v_{pre1}), causing the magnitude of the incremental quantities to approach zero and deactivating the corresponding supervising elements [11]. Thus, the maximum activation time of the protection-interoperable mode is set to t_p , after which the control scheme reverts to normal mode, regardless of the fault clearance status.

C. Overcurrent Limitation

1) Steady-state overcurrent limitation

Since the zero-sequence current is bypassed by the Δ -Y0 transformer, as shown in Fig. 6, only the positive- and negative-sequence currents are limited to ensure the phase current is within the current limitation, yielding

$$I_{t1} \leq I_{lim1}, \quad I_{t2} \leq I_{lim2} \quad (16)$$

where I_{lim1} and I_{lim2} are the current limitation values.

To limit the positive-sequence current, the corresponding virtual impedance should satisfy

$$\frac{|e_{ref1} - v_{t1}|}{I_{lim1}} \leq |Z_{v1} + jX_{f1}| \quad (17)$$

To limit the current and ensure the reliability of supervising elements, substituting (9) into (17) yields

$$\left| \frac{\overbrace{v_{tpre1} + i_{tpre1} jX_{f1}}^{\epsilon_{pre1}} + i_{tpre1} Z_{v1} - v_{t1}}{Z_{v1} + jX_{f1}} \right| \leq I_{lim1} \quad (18)$$

Based on (18), the conservative requirement for Z_{v1} is derived by

$$|Z_{v1} + jX_{f1}| \geq \frac{|v_{tpre1} - v_{t1}|}{I_{lim1} - I_{tpre1}} \quad (19)$$

To limit the negative-sequence current, the requirement for Z_{v2} is derived by

$$\frac{V_{t2}}{I_{lim2}} \leq |Z_{v2} + jX_{f2}| \quad (20)$$

Fig. 13 demonstrates the adaptive virtual inductances for positive- and negative-sequence quantities, where I_{thX1} and I_{thX2} denote the current thresholds, beyond which the adaptive virtual inductance is activated. K_{X1} and K_{X2} represent the proportional gains. To mitigate measurement noises, the LPFs,

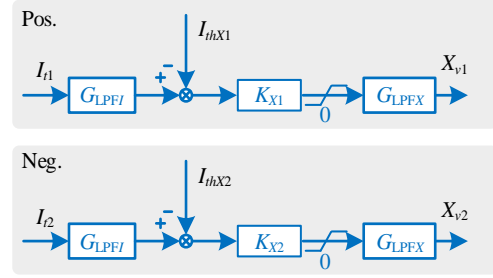


Fig. 13 Adaptive virtual inductance for positive- and negative-sequence quantities.

i.e., G_{LPF1} , are applied to the measured currents, I_{t1} and I_{t2} . To maintain small-signal stability, the first-order LPFs (G_{LPF2}) are used with the virtual inductance [19]. The virtual inductances are derived based on the respective current magnitudes, yielding

$$\begin{cases} X_{v1} = K_{X1} (I_{t1} - I_{thX1}) \\ X_{v2} = K_{X2} (I_{t2} - I_{thX2}) \end{cases} \quad (21)$$

To ensure the reliability of the supervising elements, only virtual inductances are employed. Combining (19), (20), and (21), the requirements for K_{X1} and K_{X2} are determined as

$$\begin{cases} K_{X1} \geq \frac{|v_{tpre1} - v_{t1}|}{(I_{lim1} - I_{tpre1})(I_1 - I_{thX1})} - \frac{X_{f1}}{I_1 - I_{thX1}} \\ K_{X2} \geq \frac{V_{t2}}{I_{lim2}(I_2 - I_{thX2})} - \frac{X_{f2}}{I_2 - I_{thX2}} \end{cases} \quad (22)$$

Based on (22), the values of K_{X1} and K_{X2} can be set according to the expected maximum values of $|v_{tpre1} - v_{t1}|$ and V_{t2} , respectively.

2) Transient overcurrent limitation

To meet the requirements of the supervising elements, the virtual impedance should be highly inductive, which amplifies the DC component decaying rate of the fault current and poses challenges to the transient current limitation [1]. In contrast, virtual resistance accelerates the decay of the DC component in fault currents. Therefore, incorporating virtual resistance can effectively limit transient currents. However, this conflicts with the requirements of protective relays. To address this issue, the transient virtual resistance method in [1] is employed for a maximum duration of $t_r=50$ ms, as shown in Fig. 12. At the same time, a time delay (t_r) is implemented into the protective relays, which is a common approach to addressing their poor performance during the transient period [30].

VI. IMPACT ON TRANSIENT STABILITY

This section examines the transient stability of GFM-IBRs with the proposed protection-interoperable control.

First, during the protection-interoperable mode, the APC operates in open loop, eliminating transient stability concerns. However, in the normal mode, the APC transitions to the closed-loop control, affecting the transient stability. To enhance transient stability, the adaptive fast/slow power control method described in [2] can be employed during the normal mode. In this method, the current magnitude is compared with a threshold (I_{th}) to determine whether a fast-timescale power

control is needed. When $I_{t1} \geq I_{thf}$, which indicates a huge power angle, the fast-timescale power control is implemented to avoid the loss of synchronization (LOS). Otherwise, a slow-timescale power control is applied to maintain GFM capability. Here, $I_{thf}=0.94$ p.u. according to [2]. For more details on the adaptive fast/slow power control, refer to [2].

Furthermore, the duration of protection-interoperable control mode can be limited by appropriately reducing the value of t_p , as shown in Fig. 12. This minimizes the period of continued grid-condition variations under the open-loop power control, thereby mitigating the risk of LOS when the control scheme transitions from the protection-interoperable mode back to the normal mode.

VII. HARDWARE-IN-THE-LOOP RESULTS

Fig. 14 (a) and (b) depict the actual hardware devices and the topology of the CHIL testing setup, which are used to validate the effectiveness of the proposed FRT method. Three RT-Box3 units are utilized to implement the controller, main circuit, and relay, respectively. Table I presents the parameters of the main circuit. Here, it is assumed an *ag* fault occurs between the bus 1 and the bus 2, $m=0.01$ and the fault resistance is 20Ω . To highlight the effectiveness of the proposed FRT method on the performance of supervising elements, t_p is set to 1s, thereby extending the operating duration of the supervising elements.

Fig. 15 presents the CHIL results of supervising elements under conventional power controls. The correct zones for $\Delta\delta_{21}$ and $\Delta\varphi_1$ are highlighted in blue and grey, respectively, as shown in Fig. 15 (a). When typical power control is used to regulate internal voltage, Eq. (9) does not necessarily hold, leading to deviations of $\Delta\delta_{21}$ and $\Delta\varphi_1$ from their respective bands. Fig. 15 (b) shows the CHIL results for δ_{20} , φ_2 , and φ_0 where the correct zones are highlighted in grey for δ_{20} and in blue for φ_2 and φ_0 . Since the highly inductive virtual impedance-based CLC is implemented and the Δ -Y0 transformer bypasses the direct control of the IBR for zero-sequence quantities, δ_{20} , φ_2 , and φ_0 consistently fall within their correct bands.

Fig. 16 presents the CHIL results when the proposed FRT method is implemented. In Fig. 16 (a), the correct zones for $\Delta\delta_{21}$ and $\Delta\varphi_1$ are highlighted in blue and grey, respectively. With E_{ref1} and θ_{ref1} provided based on (9), $\Delta\varphi_1$ and $\Delta\delta_{21}$ remain within the corresponding bands after fault inception, confirming the effectiveness of the proposed FRT method. In Fig. 16 (b), the correct zones for φ_2 and φ_0 are highlighted in blue, while the correct zone for δ_{20} is highlighted in grey. With the implementation of the proposed FRT method, φ_2 , φ_0 , and δ_{20} remain within their respective bands after fault inception. These CHIL results validate the effectiveness of the proposed protection-interoperable FRT method.

VIII. EXPERIMENTAL RESULTS

Fig. 17 illustrates the experimental setup used to evaluate the performance of the proposed FRT method during grid disturbances. The 45 kVA Chroma 61850 grid simulator is employed to generate grid disturbances, while the DS1007 dSPACE system is utilized to implement the proposed FRT method. The parameters of the main circuit are provided in Table II.

TABLE I
PARAMETERS OF THE MAIN CIRCUITS FOR CHIL

Symbol	Meaning	Value
v_g	Grid voltage (L-L, RMS)	220kV (1.732 p.u.)
f_1	Grid frequency	50Hz
S	Rated power	100MW (1 p.u.)
n	Turn ratio	33kV/220kV
v_{dc}	DC-link voltage	40kV
L_f	Inductance filter	5 mH
L_T	Transformer leakage inductance	77mH (0.05 p.u.)
l	Length of transmission line	100km
Z_{l1}/l	Positive-sequence line impedance	$0.03+j0.34\Omega/\text{km}$
Z_{l0}/l	Zero-sequence line impedance	$0.18+j1.19\Omega/\text{km}$
Z_g	Grid impedance	200mH (SCR=6.8)

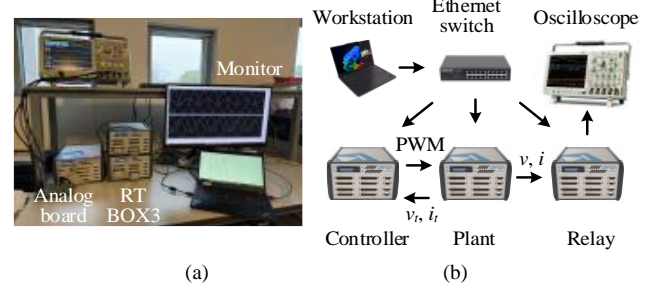


Fig. 14 CHIL testing setup. (a) Hardware devices. (b) Topology.

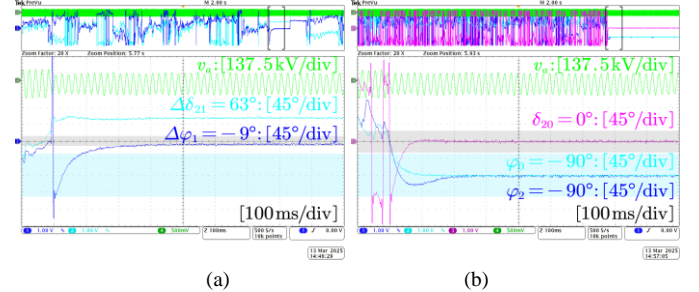


Fig. 15 CHIL results of the supervising elements under conventional power control. (a) Incremental quantity-based elements. (b) Negative-, and zero sequence quantity-based elements.

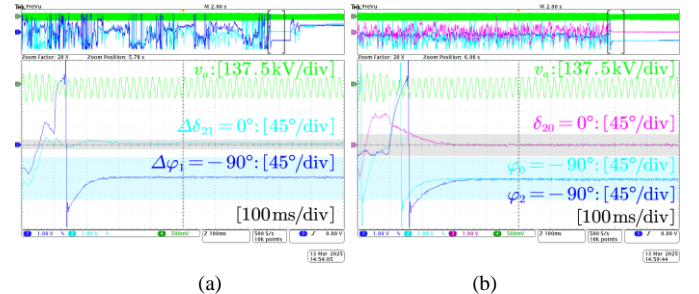


Fig. 16 CHIL results of the protective elements under the proposed FRT method. (a) Incremental quantity-based elements. (b) Negative-, and zero sequence quantity-based elements.

A. Verification of Switching Criteria

Fig. 18 presents the experimental results validating the switching criteria of the proposed FRT method, where $t_p=0.3s$. Here, if $I_{max} \geq I_{th1}$, $S_f=1$. Otherwise, $S_f=0$. Moreover, when the protection-interoperable mode is activated, $S_p=1$. ΔZ_{l1} is defined as $\Delta v_{r1}/\Delta i_{t1}$. The red and blue arrows indicate the moments of fault inception and fault clearance, respectively. When v_g drops to 0.7 p.u., the protection-interoperable mode is activated ($S_p=1$), as shown in Fig. 18. During the fault period, ΔZ_{l1} is close to -90° . After 0.2s, the fault is cleared, and the S_p

TABLE II
PARAMETERS OF THE MAIN CIRCUITS FOR EXPERIMENT

Symbol	Meaning	Value
v_g	Grid voltage (L-L, RMS)	86.6V (0.816 p.u.)
f_i	Grid frequency	50Hz
f_s	Sampling frequency	10 kHz
S	Rated power	1kW (1 p.u.)
L_g	Grid impedance	6mH (SCR=4)
L_f	Inductance filter	3mH

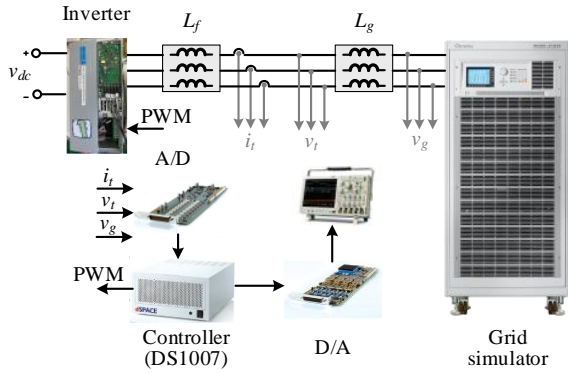


Fig. 17 Diagram of the experimental setup

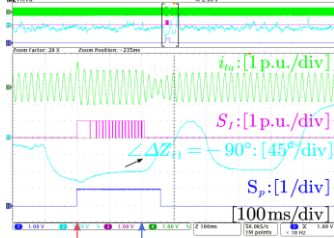


Fig. 18 Effective switching criteria when v_g drops to 0.7 p.u. for 0.2s, and $t_p=0.3s$.

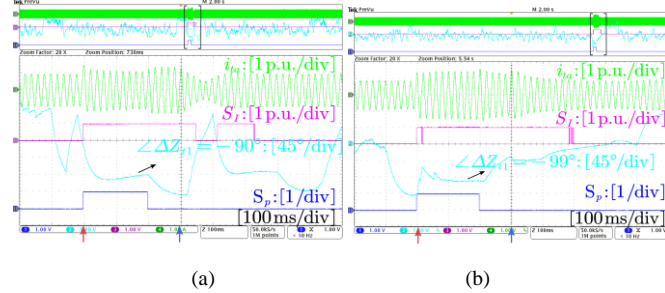


Fig. 19 Effective overcurrent limitation under grid disturbances lasting 0.3s, and $t_p=0.2s$. (a) v_g drops to 0.1 p.u. (b) v_g is subjected to a -60° phase jump.

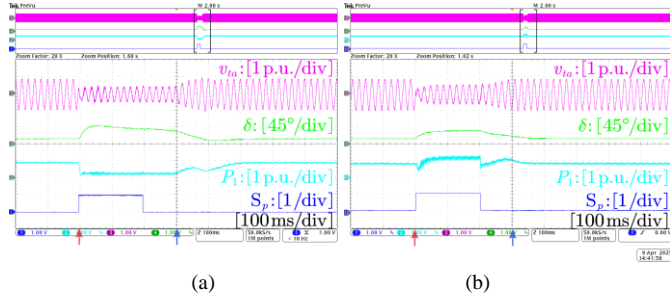


Fig. 20 Transient stability maintenance under grid disturbances lasting 0.3s and $t_p=0.2s$. (a) v_g drops to 0.1 p.u. (b) v_g is subjected to a -60° phase jump.

returns to 0 after S_f remains at 0 for a duration of t_1 (50ms). This experimental result validates the effectiveness of the proposed switching criteria.

B. Verification of Overcurrent Limiting Performance

Fig. 19 presents the experimental results for grid disturbances lasting 0.3 s, where v_g drops to 0.1 p.u., as shown in Fig. 19 (a), and a -60° phase jump occurs, as shown in Fig. 19 (b). During the fault period, $\Delta\angle Z_{f1}$ remains close to -90° with the implementation of the proposed FRT method. After t_p (0.2s) elapses, the protection-mode control is deactivated, and the control scheme transitions to the normal control mode. Under severe voltage sag and phase jump conditions, the fault current remains below 1.5 p.u. These experimental results confirm the effectiveness of the proposed FRT method in limiting fault current during severe grid disturbances.

C. Verification of Transient Stability

Fig. 20 presents the experimental results evaluating the impact of the proposed FRT method on transient stability, with $t_p=0.2s$. Here, δ is the angle difference between the POC and grid voltages. In Fig. 20 (a), v_g drops to 0.1 p.u. for a duration of 0.3s. In Fig. 20 (b), a -60° phase jump occurs and lasts for 0.3s. These experimental results show that under the implementation of the proposed FRT method, the IBR maintains transient stability under severe grid disturbances.

IX. CONCLUSION

This paper proposes a protection-interoperable FRT method to enhance the performance of the incremental quantity-based supervising elements in IBR-based systems. By modifying the power control and CLC of the GFM-IBR, the proposed method not only improves the reliability of incremental quantity-based supervising elements during the short circuit faults but also ensures effective overcurrent limitation and transient stability under grid disturbances. The effectiveness of the proposed method is validated through CHIL tests for supervising elements. Furthermore, its performance under severe grid disturbances is confirmed through experimental tests.

REFERENCES

- [1] T. Liu, X. Wang, F. Liu, K. Xin, and Y. Liu, "A current limiting method for single-loop voltage-magnitude controlled grid-forming converters during symmetrical faults," *IEEE Trans. Power Electron.*, vol. 37, no. 4, pp. 4751–4763, Apr. 2022.
- [2] H. Wu and X. Wang, "Control of grid-forming VSCs: A perspective of adaptive fast/slow internal voltage source," *IEEE Trans. Power Electron.*, vol. 38, no. 8, pp. 10151–10169, Aug. 2023.
- [3] B. Kasztenny, "Distance elements for line protection applications near unconventional sources," in *Proc. 75th Annu. Conf. Protective Relay Eng.*, College Station, TX, USA, Mar. 2022, pp. 1–18.
- [4] "Protection of 100% Inverter-dominated Power Systems with Grid-Forming Inverters and Protection Relays – Gap Analysis and Expert Interviews", Sandia National Laboratories, SAND204-04848, 2024.
- [5] *D90Plus Line Distance Protection System*, GE, Markham, ON, Canada, Mar. 2012. [Online]. Available: www.gedigitalenergy.com/products/manuals/d90plus/gek-113240b.pdf.
- [6] Z. Yang, W. Liao, C. L. Bak, and Z. Chen, "Control-based faulty phase detection methods for lines with converter-interfaced sources," *IEEE Trans. Ind. Electron.*, vol. 71, no. 7, pp. 7290–7300, Jul. 2024.
- [7] Z. Yang, Z. Liu, Q. Zhang, Z. Chen, J. D. J. Chavez, and M. Popov, "A control method for converter-interfaced sources to improve operation of directional protection elements," *IEEE Trans. Power Del.*, vol. 38, no. 1, pp. 642–654, Feb. 2023.
- [8] B. Kasztenny, M. V. Mynam, and N. Fischer, "Sequence component applications in protective relays—Advantages, limitations, and solutions," in *Proc. 72nd Annu. Conf. Protective Relay Eng. (CPRE)*, College Station, TX, USA, 2019, pp. 1–23.

- [9] P. G. McLaren, G. W. Swift, Z. Zhang, E. Dirks, R. P. Jayasinghe, and I. Fernando, "A new directional element for numerical distance relays," *IEEE Trans. Power Del.*, vol. 10, no. 2, pp. 666–675, Apr. 1995.
- [10] S. Huang, L. Luo, and K. Cao, "A novel method of ground fault phase selection in weak-infeed side," *IEEE Trans. Power Del.*, vol. 29, no. 5, pp. 2215–2222, Oct. 2014.
- [11] G. Benmouy and J. Roberts, "Superimposed quantities: their true nature and application in relays", vol. 199. Pullman, WA, USA: Schweitzer Eng. Lab., 1999.
- [12] P. M. Anderson, *Power System Protection*. New York: IEEE Press, 1999.
- [13] F. V. Lopes, M. J. B. B. Davi, M. Oleskovicz, A. Hooshyar, X. Dong, and A. A. A. Neto, "Maturity analysis of protection solutions for power systems near inverter-based resources," *IEEE Trans. Power Del.*, vol. 29, no. 5, pp. 1–14, Jun. 2024.
- [14] B. Kasztenny, "Line protective relays suitable for systems with a high penetration of unconventional sources – operating principles and field experience", . in *CGRIE Canada Conference*, 2023.
- [15] SEL-T400L Ultra-High-Speed Transmission Line Relay, SEL, July 2023. [Online]. Available: <https://selinc.com/products/T400L/docs/>.
- [16] A. Banaïmoqadam, A. Hooshyar, and M. A. Azzouz, "A control-based solution for distance protection of lines connected to converter-interfaced sources during asymmetrical faults," *IEEE Trans. Power Del.*, vol. 35, no. 3, pp. 1455–1466, Jun. 2020.
- [17] C. L. Peralta, H. P. Dang, and H. N. Villegas Pico, "Searching for grid-forming technologies that do not impact protection systems: a promising technology," *IEEE Electrific. Mag.*, vol. 12, no. 2, pp. 63–70, Jun. 2024.
- [18] A. Banaïmoqadam, A. Hooshyar, and M. A. Azzouz, "A comprehensive dual current control scheme for inverter-based resources to enable correct operation of protective relays," *IEEE Trans. Power Del.*, vol. 36, no. 5, pp. 2715–2729, Oct. 2021.
- [19] H. Wu and X. Wang, "Small-signal modeling and controller parameters tuning of grid-forming VSCs with adaptive virtual impedance-based current limitation," *IEEE Trans. Power Electron.*, vol. 37, no. 6, pp. 7185–7199, Jun. 2022.
- [20] H. Wu and X. Wang, "Design-oriented transient stability analysis of grid-connected converters with power synchronization control," *IEEE Trans. Ind. Electron.*, vol. 66, no. 8, pp. 6473–6482, Aug. 2019.
- [21] B. Fan, T. Liu, F. Zhao, H. Wu, and X. Wang, "A review of current-limiting control of grid-forming inverters under symmetrical disturbances," *IEEE Open J. Power Electron.*, vol. 3, pp. 955–969, 2022.
- [22] J. J. Grainger and W. D. Stevenson, *Power System Analysis*. New York: McGraw-Hill, 1994.
- [23] R. McDaniel and M. Thompson, "Impedance-based directional elements – why have a threshold setting?" in *75th Annual Georgia Tech Protective Relaying Conf.*, College Station, Atlanta, Georgia, 4–6 May 2022.
- [24] M. Benitez, J. Xavier, K. Smith, and D. Minshall, "Directional element design for protecting circuits with capacitive fault and load currents," in *Proc. 71st Annu. Conf. Protective Relay Eng.*, College Station, TX: IEEE, Mar. 2018, pp. 1–11.
- [25] B. Kasztenny, B. Campbell, and J. Mazereeuw, "Phase selection for single-pole tripping—Weak infeed conditions and cross-country faults," in *Proc. 27th Annu. Western Protect. Relay Conf.*, 2000, pp. 1–19.
- [26] H. Gong, X. Wang, L. Harnefors, J.-P. Hasler, and C. Danielsson, "Admittance-dissipativity analysis and shaping of dual-sequence current control for VSCs," *IEEE Trans. Emerg. Sel. Topics Power Electron.*, vol. 10, no. 1, pp. 324–335, Feb. 2022.
- [27] "Specific study requirements for grid energy storage systems," FINGRID, June 2023.
- [28] C. T. Lee, C. W. Hsu, and P. T. Cheng, "A low-voltage ride-through technique for grid-connected converters of distributed energy resources," *IEEE Trans. Ind. Appl.*, vol. 47, no. 4, pp. 1821–1832, Jul./Aug. 2011.
- [29] B. Fan and X. Wang, "Fault recovery analysis of grid-forming inverters with priority-based current limiters," *IEEE Trans. Power Electron.*, vol. 38, no. 6, pp. 1–10, Nov. 2022.
- [30] "IEEE guide for protective relay applications to transmission lines," IEEE Std C37.113™-2015, 2015.